Article

Axis-Dependent Conduction Polarity in WSi₂ Single Crystals

Karl G. Koster, Ziling Deng, Curtis E. Moore, Joseph P. Heremans, Wolfgang Windl,
and Joshua E. Goldberger*

Read Online

ACCESS | Metrics & More | Article Recommendations | Supporting Information

ABSTRACT: Materials that demonstrate axis-dependent conduction polarity enable new technologies by integrating *p*- and *n*-type functionality into a single crystal. Certain anisotropic crystal structures give rise to this behavior by having dominant electron conduction along one crystallographic direction and dominant hole conduction along another. However, only a few materials have been experimentally shown to demonstrate this unique property. Here, we identify axis-dependent conduction polarity in tetragonal α-WSi₂: a durable, thermally robust, and oxidation-resistant metal synthesized from earth-abundant elements. Two single crystals of α-WSi₂ were prepared using Xe floating zone techniques, and their anisotropic conduction properties were evaluated. Simultaneous positive and negative thermopowers measured along the [100] and [001] directions, respectively, indicate that this material exhibits axis-dependent conduction polarity, which closely matches theoretical predictions. Hall measurements also show dominant *p*-type and *n*-type conduction along these respective crystallographic directions. Heat capacity measurements indicate that the density of states of these crystals is close to that of an exact α-WSi₂ stoichiometry, confirming that this polarity anisotropy exists in relatively undoped crystals. In total, α-WSi₂ is an excellent material platform for the future exploration of potential applications of this phenomenon.
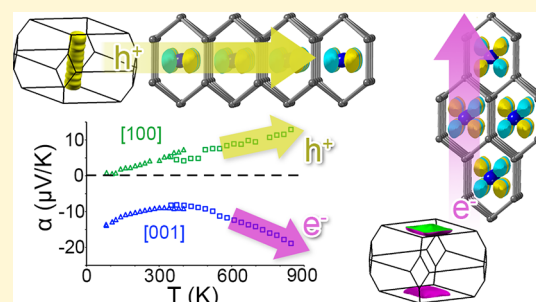
INTRODUCTION

Almost all modern electronic technologies, such as transistors, solar cells, photocatalysts, thermoelectric generators, and light-emitting diodes, rely on the integration of both *p*-type and *n*-type materials to form functional devices. Materials with axis-dependent conduction polarity simultaneously exhibit both *p*-type and *n*-type conduction behavior along different directions of a single crystal by having holes dominate conduction along one crystallographic direction and electrons along another.[1−7] These goniopolar materials have already been found to enable new device structures that overcome inefficiencies in existing technologies, such as avoiding the hot-side contacts in transverse thermoelectric generators,[2,3,8−11] enhancing the performance of cascaded Peltier coolers,[8,10,12] and allowing new phenomena such as the photogeneration of intense THz radiation in thin films.[13] While this phenomenon may enable new types of electronic devices, only a small but growing number of materials with this effect have been discovered so far.[1,2,4−7,14−16] Even fewer of these phases are air-stable and synthesized from earth-abundant elements, both of which are necessary for practical device applications and their eventual commercialization. The continued discovery of new materials with this phenomenon is essential for their long-term development.

One material with this unique effect, Re₄Si₇, has recently been shown to exhibit exceptional thermoelectric properties and remarkable efficiency in transverse thermoelectric generators.[2,3] The structure of Re₄Si₇ crystallizes into a Si-

vacancy ordered monoclinic (*Cm*) 7*a* + *c* × *b* × *c* − *a* supercell of the tetragonal *I*4/*mmm* α-WSi₂ unit cell that forms due to the strong thermodynamic preference for 14 e⁻/transition metal.[17−19] We have shown computationally that if a specific material exhibits axis-dependent conduction polarity, then isoelectronic materials with similar crystal structures are also likely to exhibit this effect. Considering that both Re₄Si₇ and α-WSi₂ feature similar bonding patterns with 14 e⁻/transition metal,[19,20] we identified WSi₂ as a potential host for axis-dependent conduction polarity. Importantly, tungsten is over 2000x more abundant in earth's crust than rhenium,[21] making α-WSi₂ much better suited than Re₄Si₇ for large-scale device applications that can exploit this phenomenon.

α-WSi₂ and the structurally identical α-MoSi₂ are historic materials that have long been studied and exploited for their electrical and thermal properties. Both materials have been used as electrical shunts and gate electrodes due to their high electrical conductivities.[22,23] Their resistance to oxidation and thermal shock, as well as high emissivity, led to their use as high-temperature heating elements[24,25] and have even made them attractive for heat shields on spacecraft reentering the
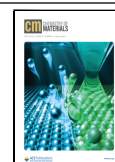
atmosphere.[26] More recently, α-MoSi$_2$ and α-WSi$_2$ have attracted significant attention after being identified as possible candidates for type II Dirac semimetals that may host topological states upon sufficient doping.[27] In contrast to the semiconducting Re$_4$Si$_7$, α-WSi$_2$ is a multiband metal,[28,29] but it still has band structure features that suggest that it will demonstrate axis-dependent conduction polarity. Early computational and de Haas−van Alphen studies elucidated the presence of multiple anisotropic Fermi surfaces, namely a nearly cylindrical prolate-shaped hole surface oriented in the z direction and a flat oblate ellipsoidal 4-cornered rosette shaped electron surface found in the $x−y$ plane.[20,30] These indicate holes should have much higher mobilities in the $x−y$ plane, and electrons should have much higher mobilities along the z-axis, both of which are signatures of axis-dependent conduction polarity.[1,20,30] More recently, low-temperature (2 K) Hall effect measurements on single crystals of WSi$_2$ showed opposite signs along different crystallographic directions. Positively sloped Hall curves were measured along the [100] direction, suggesting holes are the dominant carrier, while negatively sloped Hall curves were measured along the [001] direction, indicating electrons as the dominant carrier.[31] For these reasons, we thought it worthwhile to evaluate whether this material can host axis-dependent conduction polarity.

To investigate the possibility of axis-dependent conduction polarity in this material, we grew large single crystals of α-WSi$_2$ in a Xe floating zone furnace and fully characterized their thermal, electrical, and magnetoelectronic properties along the primary crystallographic directions. We found the crystals thermally stable up to at least 850 K and to be resistant to oxidation. We show that single crystals of WSi$_2$ demonstrate axis-dependent conduction polarity with p-type conduction along the a- and b-axes and n-type conduction along the c-axis, as evidenced by the signs of both the Seebeck and Hall coefficients. Using density functional theory (DFT) calculations and magnetoresistance measurements, we conclude that axis-dependent conduction polarity in WSi$_2$ arises via the multicarrier mechanism,[1] suggesting that electrons and holes occupy separate bands in the material. WSi$_2$ is one of the only air-stable materials with axis-dependent conduction polarity to be made from earth-abundant, nontoxic elements, highlighting its promise for large-scale production, and device implementation. The discovery of axis-dependent conduction polarity in WSi$_2$ also confirms our hypothesis[1] that once a material with axis-dependent conduction polarity is identified, it is highly likely that materials with similar structures and electron counts will demonstrate the same phenomenon.

■ RESULTS AND DISCUSSION

In tetragonal I4/mmm α-WSi$_2$, each W atom is surrounded by 10 Si atoms in a bicapped cube geometry oriented along the c-axis. Each Si atom is also bonded to 5 neighboring Si atoms in a distorted square pyramidal geometry, with each Si atom forming both the apex and the corner of two adjacent bicapped cubes (Figure 1a). This phase melts at 2160 °C,[32] so polycrystalline samples were first prepared from the elements using arc melting. Samples were prepared with 5−10% excess Si to account for the volatilization of Si during arc melting and subsequent crystal growth. The purity of this starting material was evaluated with powder X-ray diffraction. Then, this polycrystalline arc-melted material was used as feed material in a Xenon optical floating zone furnace to grow large single crystals of WSi$_2$ measuring up to 4 cm in length and 5 mm in
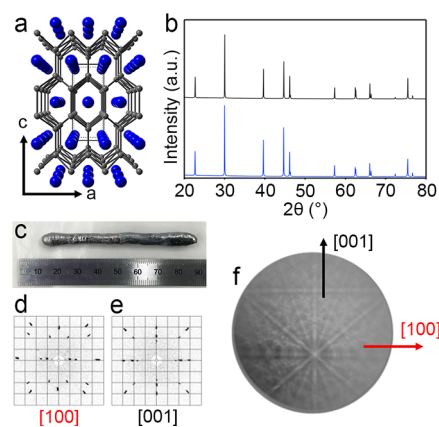

Figure 1. Crystal structure, synthesis, and orientation of WSi$_2$ single crystals. (a) Crystal structure of I4/mmm α-WSi$_2$. W atoms are shown in blue and Si atoms are shown in gray. (b) Powder X-ray diffraction pattern of α-WSi$_2$ single crystals 1 (top, black) and 2 (bottom, blue). (c) Single crystal of WSi$_2$. Laue backscattering X-ray diffraction patterns of the (d) [100] and (e) [001] directions. (f) EBSD pattern of a polished cross-sectional slice of WSi$_2$ single crystal.

diameter (Figure 1c). Powder X-ray diffraction (Figure 1b) confirmed the phase purity of the crystals, and externally performed inductively coupled plasma-atomic emission spectroscopy measurements indicated a W:Si ratio of an average stoichiometry WSi$_{1.95(2)}$ from these two crystals, which is close to the value expected for WSi$_2$ given the ±10% relative error reported for the procedure. Single crystal X-ray diffraction was also performed, and indexing and unit cell refinement of these data indicated a body-centered, tetragonal lattice belonging to the I4/mmm space group with lattice parameters ($a = b = 3.2134(1)$ Å, $c = 7.8303(4)$ Å) and atomic positions (W = 0, 0, 0 2a Wyckoff site; Si = 0, 0, 0.3347(2) 4e Wyckoff site). Refinement of atom site occupancies was consistent with full occupancy of both the tungsten and silicon sites, and the crystallographic data are summarized in Tables S1−S3.

Backscattering Laue X-ray diffraction was used to orient the crystals along the primary crystallographic directions ([001]/ [010] and [100]) (Figure 1d,e). It was found that the crystals grew along one of the equivalent [100]/[010] directions, with the other [100]/[010], and [001] directions both lying parallel to the plane of a cross-sectional slice of the rod-shaped crystal. Electron backscattering diffraction (EBSD) patterns of polished cross-sectional slices of the crystals further confirm the single-crystallinity and the relative orientations of the crystals (Figure 1f), including the [100] growth direction of both crystals. The EBSD pattern of 50 random spots across the entire 5 mm diameter cross-section was nearly identical and all indexed to the same [100] orientation, indicating that each crystal is comprised of a single domain.

The electronic structure of α-WSi$_2$ was calculated using DFT. The lattice parameters and atomic positions obtained from the Rietveld refinement of the powder X-ray diffraction pattern were used to generate band structures and their related Fermi surfaces. The band structure indicates that WSi$_2$ is metallic, with both a hole-like and electron-like band that crosses the Fermi level (Figure 2a) in the first Brillouin zone (Figure 2b). The electron pocket is a pillow-shaped oblate ellipsoid and is predominantly comprised of W 5d$_{xz}$ and 5d$_{yz}$ orbitals, suggesting that electrons will dominate conduction along the c-axis (Figure 2c,d). The hole pocket is a narrow,
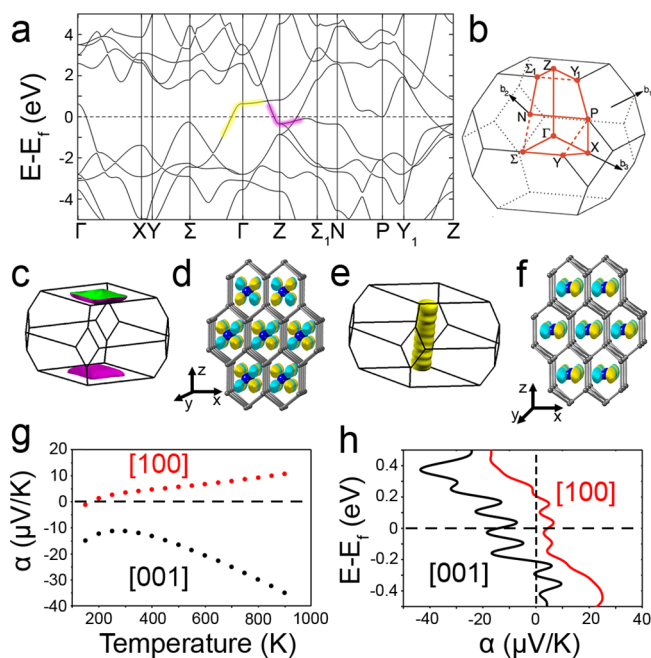
Figure 2. Calculated electronic properties of WSi₂. (a) Calculated band structure of WSi₂ with pink band corresponding to the electron pocket and yellow band corresponding to the hole pocket. (b) The body-centered tetragonal Brillouin zone for $c > a$. (c) Fermi surface and (d) wavefunction (ψ) of the bottom of the electron pocket at Z ($E - E_f = -0.48$ eV), showing the W $5d_{xz}/d_{yz}$ orbital origin. (e) Fermi surface and (f) wavefunction (ψ) of the top of the hole pocket at Γ ($E - E_f = 0.59$ eV), showing the W $5d_{xy}$ orbital origin. (g) Calculated thermopowers at $E - E_f = 0$ as a function of temperature and (h) calculated thermopowers as a function of doping level at 400 K.

cylindrically shaped prolate ellipsoid and is predominantly comprised of W $5d_{xy}$ orbitals, suggesting that holes will dominate conduction along the a- and b-axes (Figure 2e,f). The orbital composition of these two points is very similar to the conduction band minimum and valence band maximum of Re₄Si₇.[2] These calculated Fermi surfaces are consistent with

previously reported calculations and de Haas−van Alphen measurements.[20,30,31] Crystal Orbital Hamilton Population (COHP) calculations, partial density of states (pDOS), and orbitally resolved band structures confirmed the atomic orbital origins of both electron and hole conduction (Figures S1−S3). COHP calculations reveal that the bands near the Fermi level consist mostly of nonbonding orbital character. In particular, the W−Si bonding states appear at $E - E_F = -3$ eV and W−Si antibonding character appears at $E - E_F = 2$ eV. The Si−Si bonds lie much deeper in the valence band at lower energies. The low-lying Si−Si bonding states, and higher energy metal−Si bonding and antibonding states is often seen in the related 14 e⁻ per transition metal Nowotny Chimney Ladder phases.[18] The pDOS shows that the orbital composition of the valence band maximum is W $5d_{xy}$ in nature, which is also confirmed by the orbital resolved band structure. In particular, the orbitally resolved W $5d_{xy}$ band structure shows a large downward-curving energy dispersion from Γ to Σ and Γ to X, which corresponds to the [100]/[010] directions but is flat from Γ to Z, which corresponds to the [001] direction. Simultaneously, the conduction band minimum in the pDOS is comprised of W $5d_{xz}/d_{yz}$ orbitals (Figure S1) that have a strong upward-curving energy dispersion in the orbitally resolved band structure from Z to Γ (Figure S2), indicating that electrons will dominate transport along the [001] direction. Overall, these calculations suggest that WSi₂ will exhibit axis-dependent conduction polarity via the multicarrier mechanism, in which electrons and holes are both present in different bands such that electrons have a higher mobilities along one direction, and holes a higher mobility along another.[1]

Seebeck coefficient tensors (α_{xx} and α_{zz}) were derived from the electronic band structure assuming an isotropic scattering time approximation as implemented in the linear Boltzmann equation solver BoltzTraP, and further indicate the presence of axis-dependent conduction polarity. When nominally undoped at $E - E_f = 0$, α_{xx} and α_{zz} are predicted to have oppositely signed thermopowers above 200 K, with α_{xx} being positive and α_{zz} being negative (Figure 2g). At higher temperatures, the α_{xx} and α_{zz} thermopowers are generated by carriers across a wider
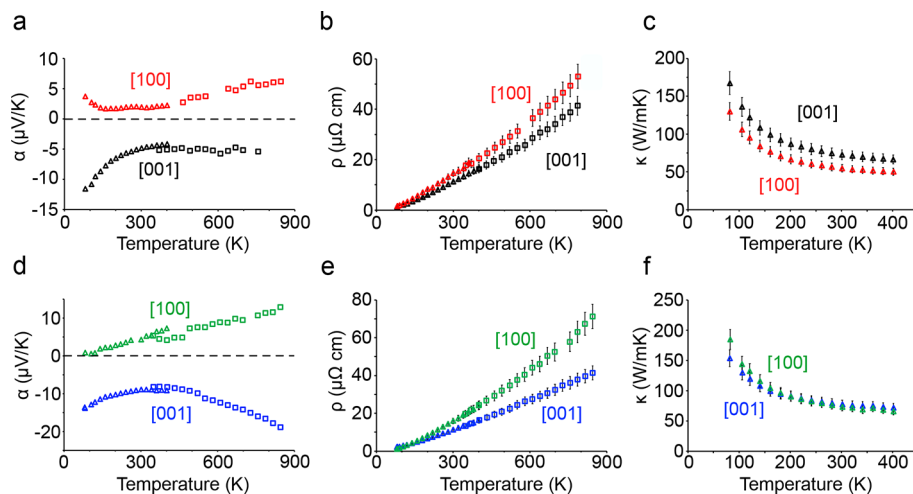

Figure 3. Thermal, electrical, and thermoelectric properties of two different WSi₂ crystals. Triangles denote data points collected using a liquid nitrogen cryostat, while squares indicate data collected using a Linseis LSR-3 instrument. (a) The thermopowers, (b) thermal conductivities, and (c) electrical resistivities of single crystal 1 of WSi₂ as a function of temperature, measured along both the [001] (black) and [100] (red) directions. (d) The thermopowers, (e) thermal conductivities, and (f) electrical resistivities of single crystal 2 of WSi₂ as a function of temperature, measured along both the [001] (blue) and [100] (green) directions.

range of energy close to E_f and are less susceptible to local changes in the band structure. The α_{xx} and α_{zz} thermopowers were also calculated from 300 to 600 K across a range of doping levels (Figures 2h and S4). These calculations indicate that α_{xx} and α_{zz} should have opposite signs near the Fermi level from $E - E_f = +0.2$ to -0.2 eV, especially at higher temperatures. It is important to point out that this axis-dependent conduction polarity occurs at $E - E_f$ far below the predicted type II Dirac point at $E - E_f = \sim 0.71$ eV.[27]

To experimentally confirm that crystals of WSi_2 demonstrate axis-dependent conduction polarity, the transport properties of two different crystals of WSi_2 were measured along the [100] and [001] crystallographic directions from 80 to 850 K (Figure 3). Special care was taken to measure along the precise [100] and [001] directions, as these correspond to the directions where the off-diagonal component of the thermoelectric tensor is zero. Positive Seebeck coefficients were measured along the [100] directions of both crystals 1 (Figure 3a) and 2 (Figure 3d) while negative Seebeck coefficients were measured along the [001] directions. At 760 K, crystal 1 had thermopowers of $+6$ μV/K along the [100] direction and -5 μV/K along the [001] direction (Figure 3a). Similarly, at 760 K, crystal 2 demonstrated thermopowers of $+11$ μV/K along the [100] direction and -16 μV/K along the [001] direction (Figure 3d). The magnitudes of these values are quite close to the thermopower values calculated from first principles in Figure 2g, especially at higher temperatures where a larger energy window of the band structure is sampled. Below 100 K in crystal 2, the thermopower along the [100] crosses from positive to negative below 80 K which is similar to the calculated crossover at 200 K (Figure 2g), while in crystal 1 the [100] turns slightly more positive below 140 K. At lower temperatures, the charge carriers with energies much closer to E_F participate in transport, magnifying any subtle deviations between the calculated and experimental band structures, as well as extrinsic doping and Fermi levels.

Both crystals demonstrate metallic resistivity trends with similar values measured for both the [100] and [001] directions (Figure 3b,e). In both crystals, the [100] resistivity is up to 70% higher than the [001] with the largest differences at the highest temperatures. At 300 K, the [100] resistivity of 14.3 $\mu\Omega$ cm is just 20% higher than the [001] resistivity of 11.2 $\mu\Omega$ cm for crystal 1. Temperature-dependent resistivity measurements were also performed from 2 to 300 K in a Physical Properties Measurement System (PPMS) (Figure S5). These data closely matched the values collected using a liquid nitrogen cryostat (Figure 3). Additionally, the residual resistivity ratio (ρ_{300K}/ρ_{2K}), was measured to be 27 for WSi_2 crystal 1 and 8.6 for crystal 2, which are indicative of relatively few grain boundaries and scattering sites in these metallic crystals, and comparable to recent reports.[27]

Both crystals have a high thermal conductivity and demonstrate relatively isotropic thermal conductivity along both the [100] and [001] directions (Figure 3c,f). The total thermal conductivity of a material is the sum of the lattice (κ_{lat}) and electronic (κ_{elec}) components. The electronic component of the thermal conductivity for both crystals along both directions can be readily estimated from the electrical resistivity using the Wiedemann−Franz law and the standard Lorenz number of 2.44×10^{-8} V^2 K^{-2}. Using this method, at 300 K, κ_{elec} along the [100] and [001] directions are 51 and 64 W m^{-1} K^{-1}, respectively for crystal 1. By subtracting κ_{elec} from the total thermal conductivity, κ_{lat} can be derived and is found

to be 4 and 8 W m^{-1} K^{-1} along the [100] and [001] directions at 300 K. For comparison, Re_4Si_7, which is two orders of magnitude more electrically resistive, and thus thermal conductivity is almost completely dominated by κ_{lat}, has a relatively isotropic total thermal conductivity of 4−4.5 W m^{-1} K^{-1} at 300 K. Thus, the lattice thermal conductivity is similar across both materials, which feature nearly identical elements in similar 3D bonding patterns. In summary, the minimal anisotropy in thermal conductivity is dictated mostly by the minimal anisotropy in κ_{elec}.

While we determined that WSi_2 exhibits axis-dependent conduction polarity using thermopowers across a wide temperature range, previous reports have determined the sign of the majority carrier at low temperature using Hall measurements.[31] These measurements hinted that WSi_2 may demonstrate axis-dependent conduction polarity, with a negative Hall coefficient along the [001] direction and a positive Hall coefficient along the [100] direction. We performed Hall measurements on crystals 1 (Figure 4a) and
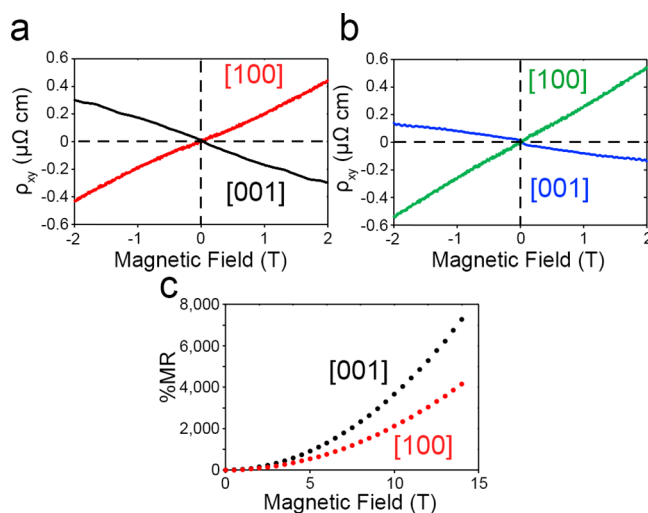

Figure 4. Hall measurements of (a) WSi_2 crystal 1 and (b) WSi_2 crystal 2 with current applied along the [100] (red, green) and [001] (black, blue) crystallographic directions at 2 K. (c) Transverse magnetoresistance of crystal 1 with current applied along the [100] (red) and [001] (black) directions at 2 K, where %MR = $[\rho(B) - \rho(0)]/\rho(0) \times 100$.

2 (Figure 4b), confirming the original result. Based on the slope from ± 1 T, crystal 1 has $R_H = -0.16$ $\mu\Omega$ cm/T along the [001] direction and $R_H = 0.21$ $\mu\Omega$ cm/T along the [100] direction. Similarly, crystal 2 has $R_H = -0.07$ $\mu\Omega$ cm/T along the [001] direction and $R_H = 0.26$ $\mu\Omega$ cm/T along the [100] direction. These values are close to previous measurements on single crystals.[31] Using a single carrier approximation, these R_H values would correspond to carrier densities in the range of 2−9×10^{21} cm^{-3}. It is important to point out that anisotropic mobility tensors in materials with axis-dependent conduction polarity precludes the direct determination of e$^-$ and h$^+$ concentrations and mobilities from Hall measurements. However, the change in sign measured along different directions suggest that holes have a higher mobility than electrons along the [100] direction, whereas electrons have a higher mobility along the [001] direction. These conclusions are supported by effective masses (m^*) calculated from the averaged curvature of the anisotropic electron and hole bands.

Along the [100] direction, $|m^*_{xx, h}| = 0.14$ m_e and $|m^*_{xx, e}| = 2.1$ m_e, suggesting that holes will dominate conduction. In the [001] direction, $|m^*_{zz, h}| = 3.7$ m_e and $|m^*_{zz, e}| = 0.73$ m_e, suggesting that electrons will dominate conduction. These values also demonstrate the greater degree of anisotropy in the hole band compared to that of the electron band, which is similarly observed in Re_4Si_7.[2] Finally, a large transverse magnetoresistance is observed (Figure 4c) along both the [100] and [001] directions, indicating that the simultaneous presence of independent electron and hole bands contribute to conduction. This is a clear signature that axis-dependent conduction polarity arises due to a multiband mechanism.[1]

Heat capacity measurements were also performed from 2 to 300 K to determine the doping level of the WSi_2 crystals (Figure 5a). At low temperature, the heat capacity of a metal
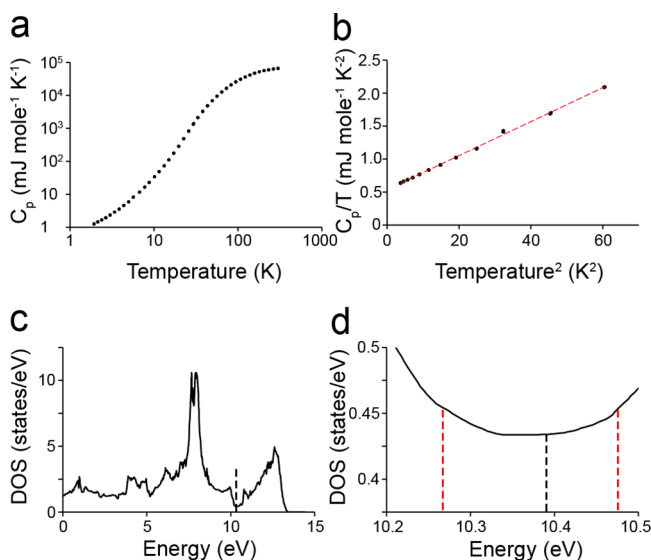

Figure 5. Specific heat capacity measurement of WSi_2. (a) Specific heat capacity of WSi_2 from 2 to 300 K. (b) Linearized specific heat capacity at low temperature. (c) Calculated density of states of a primitive WSi_2 cell with a black dashed line marking $E - E_f = 0$. (d) Expanded DOS near the Fermi level showing the possible doping range of the WSi_2 crystals based on the DOS extrapolated from the specific heat capacity measurement. The black dashed line shows the calculated undoped Fermi level, and the red dashed lines enclose the possible doping range based on the experimentally determined DOS.

can be described by $C_p = \gamma T + \beta T^3$, where γT is the electronic specific heat and βT^3 is the phonon specific heat.[33] By plotting C_p/T vs T^2 at low temperature and extrapolating the linear fit to $T^2 = 0$, we found the temperature coefficient of the electronic specific heat, γ, to equal $5.38 - 10^{-4}$ J mole^{-1} K^{-2} and the temperature coefficient of the phonon specific heat, β, to equal 2.57×10^{-5} J mole^{-1} K^{-4} (Figure 5b). Then, the γ value can be used to calculate the density of states (DOS) using the equation $N(E_F) = \left(\frac{3}{\pi^2 k_B^2(1+\lambda)}\right)\gamma$, where $N(E_F)$ is the DOS at the Fermi level, k_B is the Boltzmann constant, and λ is the electron–phonon coupling constant, which is generally nonzero for most real materials.[33] As a result, the DOS cannot be directly determined from the heat capacity. However, if λ is assumed to be zero, then the measured λ value in our WSi_2 crystal would correspond to a DOS of 0.4566 ± 0.002 filled electron states per eV at the Fermi level for each primitive WSi_2 cell. Using DFT, we also calculated the DOS for WSi_2 to

compare to our experimental result (Figure 5c). By comparing the DOS calculated from the heat capacity measurement to the DFT-calculated DOS, we estimate that the Fermi energy of the WSi_2 crystal is within 0.1 eV of the undoped Fermi energy of 10.39 eV (Figure 5d). However, it is difficult to determine precisely where the Fermi energy of the grown crystal lies because DFT calculation cannot perfectly capture the true electronic structure of a real crystal, in which defects and doping play large roles in even relatively pure crystals. Additionally, the relatively flat DOS near the Fermi level gives rise to a large uncertainty in Fermi energy, despite a relatively small uncertainty in the DOS calculated from the heat capacity measurement. However, despite the possible variation in Fermi energy due to the imprecision of this technique, little variation in physical properties, notably thermopower, would be expected across this narrow doping range (Figures 2h and S4).

CONCLUSIONS

In this study, we grew large single crystals of WSi_2 using floating zone methods and discovered the presence of axis-dependent conduction polarity in this material. Positive (p-type) thermopowers along the [100] direction and negative (n-type) thermopowers along the [001] direction reveal that holes and electrons are the majority charge carriers along the [100] and [001] directions, respectively. Positive Hall coefficients along the [100] direction and negative Hall coefficients along the [001] direction reinforce the same conclusion. These experimental results can be directly traced to the band structure signatures and Fermi surfaces that give rise to axis-dependent conduction polarity in this material, reinforcing the idea that Fermi surfaces and band structure signatures can be used to identify potential hosts for this phenomenon. WSi_2 represents one of the only air-stable materials with axis-dependent conduction polarity to be grown in large single crystals with earth-abundant elements. Additionally, the discovery of axis-dependent conduction polarity in WSi_2 provides conclusive evidence that materials that are isoelectronic and structurally similar to Re_4Si_7 will also demonstrate this unique phenomenon. Ultimately, while WSi_2's application in transverse thermoelectric energy generation is more limited than Re_4Si_7 due to its much smaller thermopowers and higher thermal conductivities, it may have much better potential in technologies that can exploit its axis-dependent conduction polarity and its metallic nature.

EXPERIMENTAL SECTION

Synthesis and Crystal Growth. Pure, polycrystalline buttons of α-WSi_2 were synthesized by arc melting stoichiometric amounts of W (99.95%, Alfa Aesar) and Si (99.999%, STREM) powder with 5–10% excess Si to account for the volatilization of Si that occurs at the high temperatures needed to congruently melt WSi_2. We used the Xenon Optical Floating Zone Furnace at the NSF PARADIM facility at Johns Hopkins University to synthesize two >5 mm diameter single crystals of WSi_2 from arc-melted, polycrystalline WSi_2. The single crystals were oriented along primary directions 100 and 001 using Laue backscattering X-ray diffraction and EBSD.

Single Crystal X-ray Diffraction. The single crystal X-ray diffraction studies were carried out on a Bruker Kappa Photon III CPAD diffractometer equipped with Mo K$_\alpha$ radiation ($\lambda = 0.71073$ Å). A $0.099 \times 0.067 \times 0.045$ mm piece of a silver block was mounted on a MiTeGen Micromount with Paratone 24EX oil. Data were collected in a nitrogen gas stream at 100(2) K using ϕ and ϖ scans. The crystal-to-detector distance was 60 mm using variable exposure

time (1−5 s) depending on θ with a scan width of 1.0°. The data collection was 100% complete to 37.50° in θ (0.58 Å). A total of 1847 reflections were collected covering the indices, $-5 \leq h \leq 5$, $-5 \leq k \leq 5$, $-13 \leq l \leq 13$. 87 reflections were found to be symmetry independent, with a R_{int} of 0.0331. The data were integrated using the Bruker SAINT software program and scaled using the SADABS software program. A complete phasing model for refinement was produced through solution by dual-space method (SHELXT).[34,35] All atoms were refined anisotropically by full-matrix least-squares (SHELXL-2014).[36] The crystallographic data was deposited into the CCDC under deposition number 2259109.

Materials Measurement. Crystal slices were cut from the rod-shaped single crystal using a diamond wire saw and were polished using 3 μm diamond grit suspended in oil followed by 0.05 μm alumina slurry on a precision lapping and polishing machine. These slices were cut into thin bars along the primary crystallographic directions [100] and [001]. The Seebeck coefficients, electrical resistivities, and thermal conductivities of the WSi_2 crystals were measured along the [100] and [001] directions from 80 to 400 K in a Janis liquid nitrogen vacuum cryostat. A four-probe measurement geometry was used to measure sample resistance. To measure the thermopowers of these samples, an electrical current was passed through a 120 Ω Omega strain gauge attached to one end of the sample to create a temperature gradient along the direction of the crystal being measured. Two type T thermocouples, one placed near the hot side of the sample and one placed near the cold side of the sample, measured the resulting temperature gradient and the Seebeck voltage created across the sample. Thermal and electrical contacts were made to the sample's surface using Transene GE-40 gold-epoxy paste. Percent error was calculated in the resistivity and thermal conductivity measurements by dividing the electrical contact width by the length of the sample. The Seebeck coefficients and resistivities of the single crystals were measured from 350 to 850 K using a Linseis LSR-3 instrument. The temperature-dependent resistivity measurements were performed from 2 to 300 K on the same samples using a Quantum Design 14 T Physical Properties Measurement System (PPMS), and low-temperature Hall effect measurements were performed using a Quantum Design 9 T PPMS. Heat capacity measurements were performed in the Quantum Design 9 T PPMS from 2 to 300 K.

Calculations. The DFT calculations were performed on a WSi_2 primitive cell within the Vienna Ab initio Simulation Package (VASP)[37] using Perdew−Burke−Ernzerhof (PBE) functionals.[38] The relaxed configuration was obtained using a 4 × 4 × 4 k-point grid and a plane-wave energy cutoff of 400 eV. The lattice parameters were fixed to experimental values obtained from the Rietveld refinement of the powder X-ray diffraction pattern to generate the electronic band structures and Fermi surfaces. The linear Boltzmann equation solver BoltzTraP[39] was used to calculate the Seebeck coefficient tensors of the WSi_2 conventional unit cell. In this calculation, the k-point mesh was increased to 25 × 25 × 10. Crystal Orbital Hamiltonian Population analysis was performed using LOBSTER.[40−43]

ASSOCIATED CONTENT

Ⓢⓘ Supporting Information

The Supporting Information is available free of charge at https://pubs.acs.org/doi/10.1021/acs.chemmater.3c00183.

> Crystal Orbital Hamilton Population (COHP) calculations, partial density of states (pDOS), orbitally resolved band structures, thermopower as a function of doping level and temperature, longitudinal resistivity measurements from 2 to 300 K, and crystal structure data (PDF)

AUTHOR INFORMATION

Corresponding Author

Joshua E. Goldberger − *Department of Chemistry and Biochemistry, The Ohio State University, Columbus, Ohio 43210, United States;* ⓞ orcid.org/0000-0003-4284-604X; Email: goldberger@chemistry.ohio-state.edu

Authors

Karl G. Koster − *Department of Chemistry and Biochemistry, The Ohio State University, Columbus, Ohio 43210, United States*

Ziling Deng − *Department of Materials Science and Engineering, The Ohio State University, Fontana Laboratories, Columbus, Ohio 43210, United States*

Curtis E. Moore − *Department of Chemistry and Biochemistry, The Ohio State University, Columbus, Ohio 43210, United States;* ⓞ orcid.org/0000-0002-3311-7155

Joseph P. Heremans − *Department of Mechanical and Aerospace Engineering, The Ohio State University, Columbus, Ohio 43210, United States*

Wolfgang Windl − *Department of Materials Science and Engineering, The Ohio State University, Fontana Laboratories, Columbus, Ohio 43210, United States*

Complete contact information is available at:
https://pubs.acs.org/10.1021/acs.chemmater.3c00183

Author Contributions

K.G.K. synthesized the WSi_2 single crystals, collected all experimental data presented here, and wrote the manuscript with input from J.E.G. and J.P.H. Single crystal structure solution was performed by C.E.M. Z.D. calculated the electronic structure and predicted properties of WSi_2 under the supervision of W.W.

Notes

The authors declare no competing financial interest.

REFERENCES

(1) Wang, Y.; Koster, K. G.; Ochs, A. M.; Scudder, M. R.; Heremans, J. P.; Windl, W.; Goldberger, J. E. The Chemical Design Principles for Axis-Dependent Conduction Polarity. *J. Am. Chem. Soc.* **2020**, *142*, 2812−2822.

(2) Scudder, M. R.; He, B.; Wang, Y.; Rai, A.; Cahill, D. G.; Windl, W.; Heremans, J. P.; Goldberger, J. E. Highly Efficient Transverse Thermoelectric Devices with Re4Si7 Crystals. *Energy Environ. Sci.* **2021**, *14*, 4009−4017.

(3) Scudder, M. R.; Koster, K. G.; Heremans, J. P.; Goldberger, J. E. Adiabatic and Isothermal Configurations for Re4Si7 Transverse Thermoelectric Power Generators. *Appl. Phys. Rev.* **2022**, *9*, 21420.

(4) Arguilla, M. Q.; Katoch, J.; Krymowski, K.; Cultrara, N. D.; Xu, J.; Xi, X.; Hanks, A.; Jiang, S.; Ross, R. D.; Koch, R. J.; Ulstrup, S.; Bostwick, A.; Jozwiak, C.; McComb, D. W.; Rotenberg, E.; Shan, J.; Windl, W.; Kawakami, R. K.; Goldberger, J. E. NaSn2As2: An Exfoliatable Layered van Der Waals Zintl Phase. *ACS Nano* **2016**, *10*, 9500−9508.

(5) He, B.; Wang, Y.; Arguilla, M. Q.; Cultrara, N. D.; Scudder, M. R.; Goldberger, J. E.; Windl, W.; Heremans, J. P. The Fermi Surface Geometrical Origin of Axis-Dependent Conduction Polarity in Layered Materials. *Nat. Mater.* **2019**, *18*, 568−572.

(6) Koster, K. G.; Wang, Y.; Scudder, M. R.; Moore, C. E.; Windl, W.; Goldberger, J. E. Synthesis and Characterization of a New Family of Layered PbxSn4−xAs3 Alloys. *J. Mater. Chem. C* **2021**, *9*, 6477−6483.

(7) Ochs, A. M.; Gorai, P.; Wang, Y.; Scudder, M. R.; Koster, K.; Moore, C. E.; Stevanovic, V.; Heremans, J. P.; Windl, W.; Toberer, E. S.; Goldberger, J. E. Computationally Guided Discovery of Axis-Dependent Conduction Polarity in NaSnAs Crystals. *Chem. Mater.* **2021**, *33*, 946−951.

(8) Tang, Y.; Cui, B.; Zhou, C.; Grayson, M. P × N-Type Transverse Thermoelectrics: A Novel Type of Thermal Management Material. *J. Electron. Mater.* **2015**, *44*, 2095−2104.

(9) Grayson, M.; Shao, Q.; Cui, B.; Tang, Y.; Yan, X.; Zhou, C. Introduction to (p × n)-Type Transverse Thermoelectrics. In *Bringing Thermoelectricity into Reality*, 2018; pp 81−100.

(10) Goldsmid, H. J. Application of the Transverse Thermoelectric Effects. *J. Electron. Mater.* **2011**, *40*, 1254−1259.

(11) Uchida, K.; Heremans, J. P. Thermoelectrics: From Longitudinal to Transverse. *Joule* **2022**, *6*, 2240−2245.

(12) Zhou, C.; Tang, Y.; Grayson, M. P x N-Type Transverse Thermoelectrics: An Alternative Peltier Refrigerator with Cryogenic Promise. In *Proc.SPIE*, 2014; Vol. *9000*, p 900006.

(13) Yordanov, P.; Priessnitz, T.; Kim, M.-J.; Cristiani, G.; Logvenov, G.; Keimer, B.; Kaiser, S. Intense Terahertz Radiation via the Transverse Thermoelectric Effect. 2 August 2022. *arXiv*, 2208.01480. (accessed January 15, 2023).

(14) Nakamura, N.; Goto, Y.; Mizuguchi, Y. Axis-Dependent Carrier Polarity in Polycrystalline NaSn2As2. *Appl. Phys. Lett.* **2021**, *118*, No. 153903.

(15) Felser, C.; Finckh, W. E.; Kleinke, H.; Rocker, F.; Tremel, W. Electronic Properties of ZrTe3. *J. Mater. Chem.* **1998**, *8*, 1787−1798.

(16) Dolinšek, J.; Komelj, M.; Jeglič, P.; Vrtnik, S.; Stanić, D.; Popčević, P.; Ivkov, J.; Smontara, A.; Jagličić, Z.; Gille, P.; Grin, Y. Anisotropic Magnetic and Transport Properties of Orthorhombic Al13Co4. *Phys. Rev. B* **2009**, *79*, No. 184201.

(17) Fredrickson, D. C.; Lee, S.; Hoffmann, R.; Lin, J. The Nowotny Chimney Ladder Phases: Following the Cpseudo Clue toward an Explanation of the 14 Electron Rule. *Inorg. Chem.* **2004**, *43*, 6151−6158.

(18) Fredrickson, D. C.; Lee, S.; Hoffmann, R. The Nowotny Chimney Ladder Phases: Whence the 14 Electron Rule? *Inorg. Chem.* **2004**, *43*, 6159−6167.

(19) Fredrickson, D. C.; Boström, M.; Grin, Y.; Lidin, S. Re4Si7, First in a New MoSi2-Based Family of 14-Electron Phases. *Chem. −Eur. J.* **2009**, *15*, 8108−8112.

(20) Andersen, O. K.; Jepsen, O.; Antonov, V. N.; Antonov, V. N.; Yavorsky, B. Y.; Perlov, A. Y.; Shpak, A. P. Fermi Surface, Bonding, and Pseudogap in MoSi2. *Phys. B* **1995**, *204*, 65−82.

(21) Tan, L.; Chi-lung, Y. Abundance of Chemical Elements in the Earth's Crust and Its Major Tectonic Units. *Int. Geol. Rev.* **1970**, *12*, 778−786.

(22) Miller, R. J. Resistivity and Oxidation of Tungsten Silicide Thin Films. *Thin Solid Films* **1980**, *72*, 427−432.

(23) Geipel, H. J.; Hsieh, N.; Ishaq, M. H.; Koburger, C. W.; White, F. R. Composite Silicide Gate Electrodes—Interconnections for VLSI Device Technologies. *IEEE Trans. Electron Devices* **1980**, *27*, 1417−1424.

(24) Erich, F. Work Pieces for High Temperature Operation and Method of Making Them. US2902392A, 1959.

(25) Jiang, W.; Tsuji, K.; Uchiyama, T. Molybdenum Disilicide Heating Element and Its Production Method. EP0886458A2 1998.

(26) Shao, G.; Lu, Y.; Hanaor, D. A. H.; Cui, S.; Jiao, J.; Shen, X. Improved Oxidation Resistance of High Emissivity Coatings on Fibrous Ceramic for Reusable Space Systems. *Corros. Sci.* **2019**, *146*, 233−246.

(27) Pavlosiuk, O.; Swatek, P. W.; Wang, J.-P.; Wiśniewski, P.; Kaczorowski, D. Giant Magnetoresistance, Fermi-Surface Topology, Shoenberg Effect, and Vanishing Quantum Oscillations in the Type-II Dirac Semimetal Candidates MoSi2 and WSi2. *Phys. Rev. B* **2022**, *105*, 75141.

(28) Nava, F.; Mazzega, E.; Michelini, M.; Laborde, O.; Thomas, O.; Senateur, J. P.; Madar, R. Analysis of the Electrical Resistivity of Ti, Mo, Ta, and W Monocrystalline Disilicides. *J. Appl. Phys.* **1989**, *65*, 1584−1590.

(29) Bhattacharyya, B. K.; Bylander, D. M.; Kleinman, L. Fully Relativistic Self-Consistent Energy Bands of WSi2. *Phys. Rev. B* **1985**, *31*, 5462−5464.

(30) Itoh, S. Fermi Surfaces of Tungsten Silicide Alloys. *J. Phys.: Condens. Matter* **1990**, *2*, 3747.

(31) Mondal, R.; Sasmal, S.; Kulkarni, R.; Maurya, A.; Nakamura, A.; Aoki, D.; Harima, H.; Thamizhavel, A. Extremely Large Magneto-resistance, Anisotropic Hall Effect, and Fermi Surface Topology in Single-Crystalline WSi2. *Phys. Rev. B* **2020**, *102*, No. 115158.

(32) Physical Constants of Inorganic Compounds. In *CRC Handbook of Chemistry and Physics*; Lide, D. R., Ed.; CRC Press, 2009; pp 4−96.

(33) Beck, P. A.; Claus, H. Density of States Information from Low Temperature Specific Heat Measurements. *J. Res. Natl. Bur. Stand. Sect. A, Phys. Chem.* **1970**, *74A*, 449−454.

(34) Sheldrick, G. M. SHELXT − Integrated Space-Group and Crystal-Structure Determination. *Acta Crystallogr. A* **2015**, *71*, 3−8.

(35) Sheldrick, G. M. A Short History of SHELX. *Acta Crystallogr. A* **2008**, *64*, 112−122.

(36) Sheldrick, G. M. Crystal Structure Refinement with SHELXL. *Acta Crystallogr., Sect. C: Struct. Chem.* **2015**, *71*, 3−8.

(37) Kresse, G.; Furthmüller, J. Efficient Iterative Schemes for Ab Initio Total-Energy Calculations Using a Plane-Wave Basis Set. *Phys. Rev. B* **1996**, *54*, 11169−11186.

(38) Blöchl, P. E. Projector Augmented-Wave Method. *Phys. Rev. B* **1994**, *50*, 17953−17979.

(39) Madsen, G. K. H.; Singh, D. J. BoltzTraP. A Code for Calculating Band-Structure Dependent Quantities. *Comput. Phys.* **2006**, *175*, 67−71.

(40) Deringer, V. L.; Tchougréeff, A. L.; Dronskowski, R. Crystal Orbital Hamilton Population (COHP) Analysis As Projected from Plane-Wave Basis Sets. *J. Phys. Chem. A* **2011**, *115*, 5461−5466.

(41) Dronskowski, R.; Bloechl, P. E. Crystal Orbital Hamilton Populations (COHP): Energy-Resolved Visualization of Chemical Bonding in Solids Based on Density-Functional Calculations. *J. Phys. Chem.* **1993**, *97*, 8617−8624.

(42) Maintz, S.; Deringer, V. L.; Tchougréeff, A. L.; Dronskowski, R. Analytic Projection from Plane-Wave and PAW Wavefunctions and Application to Chemical-Bonding Analysis in Solids. *J. Comput. Chem.* **2013**, *34*, 2557−2567.

(43) Maintz, S.; Deringer, V. L.; Tchougréeff, A. L.; Dronskowski, R. LOBSTER: A Tool to Extract Chemical Bonding from Plane-Wave Based DFT. *J. Comput. Chem.* **2016**, *37*, 1030−1035.